Materials and Design 193 (2020) 108793

Contents lists available at ScienceDirect

Materials and Design

journal homepage: www.elsevier.com/locate/matdes

Evolution of twinning and shear bands in magnesium alloys during rolling at room and cryogenic temperature

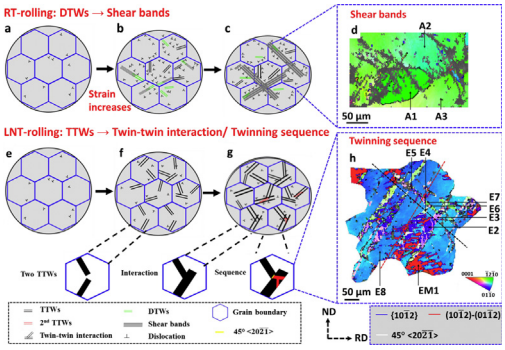
Kai Zhang [a], Jing-Hua Zheng [a,*], Yan Huang [b], Catalin Pruncu [a], Jun Jiang [a]

[a] Department of Mechanical Engineering, Imperial College London, Exhibition Road, London SW7 2AZ, UK
[b] BCAST, Institute of Materials and Manufacturing, Brunel University London, Uxbridge UB8 3PH, UK

HIGHLIGHTS

- A new twinning sequence, namely primary twin-twin interactions → secondary twin-twin interactions, was discovered.
- The rolling at cryogenic temperature was accommodated by tension twins → twin-twin interactions → twinning sequence.
- Regarding rolling at room temperature, the deformation was governed by double twins → shear bands.
- The geometrically necessary dislocation density was high in twin-twin interactions, twinning sequence and shear bands.

GRAPHICAL ABSTRACT



ARTICLE INFO

Article history:
Received 9 April 2020
Received in revised form 1 May 2020
Accepted 7 May 2020
Available online 19 May 2020

Keywords:
Twinning
Shear bands
Cryogenic rolling
EBSD
Magnesium alloys

ABSTRACT

Twinning and shear bands are two main deformation structures in magnesium alloys at low temperatures, however, the relationship between these two deformation structures is still under debate. To clarify their relationship and behaviours at low temperatures, rolling tests to various thickness reductions at room temperature (RT) and liquid nitrogen temperature (LNT) were conducted for AZ31 magnesium alloys. The evolutions of shear bands and twinning, and their interactions with geometrically necessary dislocation (GND), were observed during the RT- and LNT-rolling process. Abundant shear bands, evolving from $\{10\bar{1}1\}$-$\{10\bar{1}2\}$ double twins (DTWs), were observed in the RT-rolled samples, while a high quantity of twins, including $\{10\bar{1}2\}$ tension twins (TTWs), twin-twin interactions and twinning sequence, were observed in the LNT-rolled samples. More importantly, a rarely observed twinning sequence behaviour, namely primary TTW-TTW interactions→ secondary TTW-TTW interactions, creating a 45° $<20\bar{2}1>$ misorientation peak, was studied. Abundant GNDs accumulated around these twin-twin interactions, twinning sequence, DTWs and shear bands, while the GND density was low around TTWs. This research delivers a systematic investigation into the deformation structures in Mg alloys during the rolling process from RT to cryogenic temperature and provides insights into the newly discovered twinning sequence and twin-twin interactions.

© 2020 The Authors. Published by Elsevier Ltd. This is an open access article under the CC BY license (http://creativecommons.org/licenses/by/4.0/).

1. Introduction

Magnesium alloys attract substantial interests from automotive industries due to its low density and high specific strength [1–4]. However, the application of magnesium alloys plates is limited due to their

* Corresponding author.
E-mail address: Jinghua.zheng13@imperial.ac.uk (J.-H. Zheng).

https://doi.org/10.1016/j.matdes.2020.108793
0264-1275/© 2020 The Authors. Published by Elsevier Ltd. This is an open access article under the CC BY license (http://creativecommons.org/licenses/by/4.0/).

poor formability and high cost during the rolling process. This motivates the needs to understand their deformation behaviours and microstructures in the rolling process of Mg alloys. Shear bands and deformation twins are the dominant deformation features of the microstructure during the rolling process [5]. The twins and shear bands behaviours can have profound effects on plastic anisotropy and flow stress, and are also considered as the primary factors that trigger cracking, void formation and coalesce to failure, limiting the formability of Mg alloys plates [6–8]. Therefore, a deep understanding of the deformation structures, especially the relationships and evolution of shear bands and twins during the rolling process, is essential to reveal the deformation essence of Mg alloys.

Shear bands generally show non-crystallographic orientations, could pass through several grains or even extend through the specimen [9]. The shear bands contain intense shear strains, resulting in localization, and it could be related to the persistent and coarse slips bands at micro-scale localised deformation while it could result in material instability at macro-scale [10–12]. The generation of shear bands may be associated with localised dislocation slip, [13,14], or the localised twinning and grain boundary sliding [9]. The formation of shear bands in magnesium alloys was generated from the deformation twins [7,15] or the dynamic recrystallisation (DRX) near grain boundaries [16,17]. Compression twin (CTW) and DTW will reorient the grains to more favourable orientations for basal slips by 56° and 38°, respectively, and further deformation will result in the connection of these newly formed twins and form the shear bands [7,18]. The dislocation density is generally high around the shear bands as shear bands contain intensive shear strains providing extensive internal misorientations [19]. However, because of the complexity of dislocations and deformation twins, the origin of shear bands formation in magnesium alloys is still unclear.

Due to the lack of sufficient slip systems in magnesium, deformation twins are often generated to accommodate homogeneous plastic deformation [20–22]. TTWs are easily activated to accommodate plastic deformation, as its critical resolved shear stress (CRSS) is commonly lower than that of non-basal slip systems [5,23,24]. TTW can be generated on any one of six $\{10\bar{1}2\}$ planes in a grain. These twin variants on different planes would impinge on one another to form three types of twin boundaries, including $(10\bar{1}2)$-$(01\bar{1}2)$, $(10\bar{1}2)$-$(\bar{1}012)$, $(10\bar{1}2)$-$(0\bar{1}12)$ [21], identified as twin-twin interactions. The interactions were classified into two types: (i) co-zone twin-twin interactions for two twin variants sharing the same $<11\bar{2}0>$ zone axis [25] and (ii) non-cozone twin-twin interactions for two twin variants with different zone axes [26,27]. A 3D full-field crystal plasticity model and large-scale molecular dynamics indicated that the local stress fields were generated after the initial formation of the twin-twin interactions. This stress field promotes the twin thickening and also contributes to the nucleation of new twins [25]. Additionally, the stress fields of the twin-twin interactions are suggested to have a higher strengthening effect on the material [25,26] compared to the grains containing a single twin [28]. Currently, it has been found that changing the strain paths can maximise the volume of twin-twin interactions, providing clear development of twin-twin interactions [26,27]. While it is not known whether there are other effective methods to maximise the generation of twin-twin interactions.

Twinning sequence, forming subsequent twins in existing twins, may also occur to accommodate the imposed plastic deformation. For magnesium, the frequent twinning sequence is $\{10\bar{1}1\}$-$\{10\bar{1}2\}$ DTWs, i.e. secondary TTWs form in primary compression twins (CTWs) [29,30]. However, the formation of sequential TTWs was rarely reported in Mg alloys due to the difficulty in activating the secondary TTW in the primary TTW [31]. Until now, only few research have observed a sequential TTW in Mg-0.3 at.%Al alloy and AZ31 [32–34], which was activated by multiaxial deformation, e.g. a compression at RT in the rolling direction followed by a subsequent compression in transversion direction [31]. However, the relationships between the sequential TTWs and TTW-TTW interactions, and the concurrent interactions with dislocations, were still not clearly studied. Additionally, it is unclear whether other processing conditions can also trigger the formation of both sequential TTWs and TTW-TTW interactions.

Cryogenic rolling (cryo-rolling) would be a potential way to promote twinning activities and trigger some rare twinning behaviours, such as twin-twin interactions, twinning sequence in Mg alloys. At lower temperatures, the CRSS for dislocation slip, especially prismatic and pyramidal slip, increases substantially, while the CRSS for twinning is almost independent of temperature [35–40]. Hence, deformation twins will be the important plastic deformation structure at the cryogenic temperature [41–43]. This will enable a clear identification on the twinning formation, evolution and their relationships with dislocation during the deformation. As a comparison, the microstructure evolution during the rolling at RT was also studied to explore the origin of the shear bands formation.

In this study, AZ31 samples are rolled to various thicknesses at room and cryogenic temperatures (i.e. liquid nitrogen temperature). The microstructures are characterised using the Electron Backscatter Diffraction (EBSD) technique and optical microscopy. The main aims are: (i) investigate the relationship between shear bands and deformation twins in the RT- and LNT-rolling process; (ii) identify and analyse the rarely observed twin-twin interactions, twinning sequence and their interactions in LNT-rolling process in details, integrating the understanding.

2. Experimental method

2.1. Materials

AZ31 cast billets were provided by Magnesium Elektron. The AZ31 alloy is a commonly used magnesium alloy, mainly containing aluminium and zinc. The chemical composition of the AZ31 is presented in Table 1. The as-received AZ31 samples are in T4 heat-treated condition. The T4 heat treatment consisted of heating the samples for 4 h at 385 °C followed by 12 h at 420 °C.

2.2. Rolling at room and cryogenic temperature

A schematic illustration of the RT and LNT-rolling process is given in Fig. 1. Rectangular samples with a thickness, width and length of 3, 8 and 25 mm, respectively, were manufactured from the as-received AZ31 alloys. These samples were rolled at a moderate rolling speed of ~4.9–6.9 m/min, using a DRM C130 or Durston FSM200 rolling mill machine, for 1, 2 and 3 passes to achieve a total thickness reduction (TR) of 3%, 9% and 13%, respectively. For the LNT-rolling process, the samples were immersed in liquid nitrogen for at least 30 min to ensure the entire sample reaches the target liquid nitrogen temperature (i.e. 77 K) before each pass. Then, the immersed samples were rapidly transferred to the rolling mill machine to achieve the designed TR for each pass.

2.3. Microstructure characterisation

The 3% and 13% rolled samples with the surface of RD × ND were prepared for microscopic examination. In preparation for the microstructure observation, the rolled samples were mechanically polished using P4000 SiC grinding papers and OPS suspension. Then, the samples were chemically-etched using a mixed solution of 1 ml nitric acid, 1 ml acetic acid, 1 ml oxalic acid and 150 ml water for about 30 s. The optical

Table 1
Chemical composition (wt%) of AZ31.

	Mg	Fe	Mn	Zn	To	Al	Ca	Ni	Si	Cu
AZ31	Bal.	0.004	0.32	0.95	<0.3	3.1	<0.005	0.0006	0.02	<0.0005

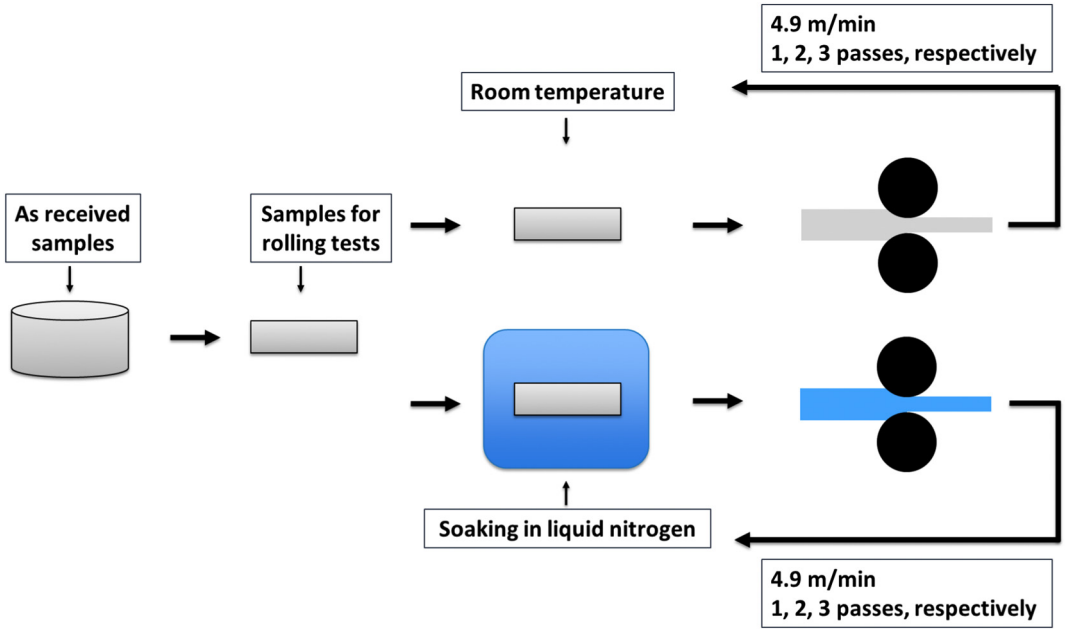


Fig. 1. Schematic diagram of the experimental rolling processes.

metallographic examination was performed on the etched samples using the Zeiss microscope, aiming to obtain large microstructure maps, with respect to various deformation levels and temperatures.

A Hitachi SEM microscope with a Bruker e-Flash HR detector connected to a smart Quantax Esprit 2.1 system was used for the EBSD observation, aiming to thoroughly examine the crystallographic morphology, identifying the twinning types, misorientation distributions, etc., and revealing the evolved deformation structures. Due to the large grain size formed in casting, a 16 μm step size was selected to characterise the grain size and texture of the as-received sample, while a 2 μm step size was used to examine the more detailed microstructures in the rolled samples.

The obtained EBSD data was subsequently analysed using HKL CHANNEL 5 software. The grain size was calculated with a critical misorientation of 5° and a minimum grain area of 10 pixels, excluding grain boundaries. Different twin boundaries were highlighted with various colours. The Kernel Average Misorientation (KAM) was calculated using the average misorientation between the probed pixel and its 5×5 surrounding pixels [44].

The as-received cast AZ31 sample was characterised by the EBSD technique. Fig. 2(a) shows the inverse pole figure (IPF) map, the grain size is relatively large but homogeneously distributed. The statistic grain size analysis is shown in Fig. 2(c). The average grain size of ~279 μm was measured. The associated texture is shown in Fig. 2(b) in which, as expected, a weak and scattered texture is observed in this cast sample.

3. Experimental results

3.1. Microstructures of AZ31 during RT-rolling and LNT-rolling process

Fig. 3(a) and (b) shows the optical microscope characterised microstructure of AZ31 samples after the RT-rolling process. Abundant black bands were observed, and those that crossed the grain boundaries (GBs) were identified as shear bands (annotated in Fig. 3(b)). The quantity of these black bands notably increased with the increase in the deformation levels from 3% to 13%, which is in good agreement with that in the literature [5,45]. With a TR =3% (Fig. 3(a)), these black bands were short and thin, and were mainly found inside of the grains. When TR increased to 13%, these black bands became thickened and bent, which crossed the GBs and, thus, considered as shear bands. It is clearly demonstrated in Fig. 3(a) and (b) that the density of the shear bands increased with higher TR values.

Fig. 3(c) and (d) present the microstructures of the AZ31 during the LNT-rolling process. The short and straight grey lines could be deformation twins, which are further confirmed by the EBSD observations in Figs. 4–9. At TR = 3%, more twins were observed in the LNT-rolled sample in Fig. 3(c), compared to that in the RT-rolled sample (Fig. 3(a)). As TR increased to 13%, (Fig. 3(d)), the density of twins in the LNT-rolled sample increased, and these twin boundaries intersected and tangled with each other. Almost no shear bands were observed in the LNT-rolled sample. It may be noted that few micro-cracks were observed near the grain boundaries in the LNT-deformed sample (Fig. 3(d)), which may be attributed to the stress concentration around the grain

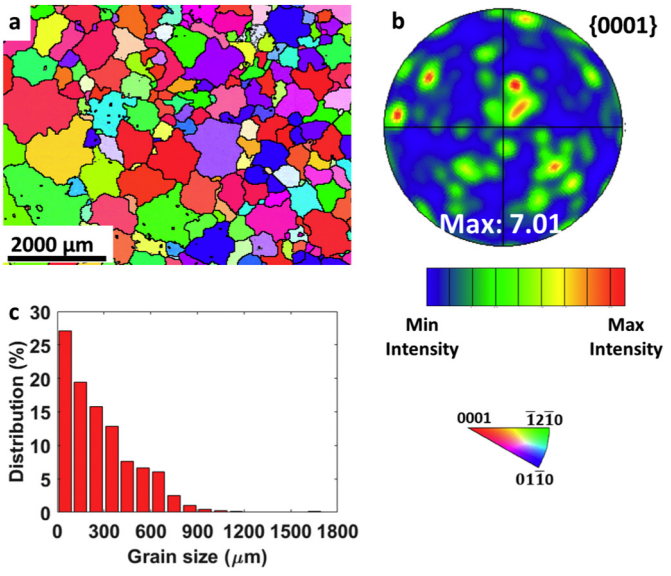


Fig. 2. (a) EBSD IPF image, (b) {0001} pole figure and (c) the grain size distribution map of the as-received AZ31 sample.

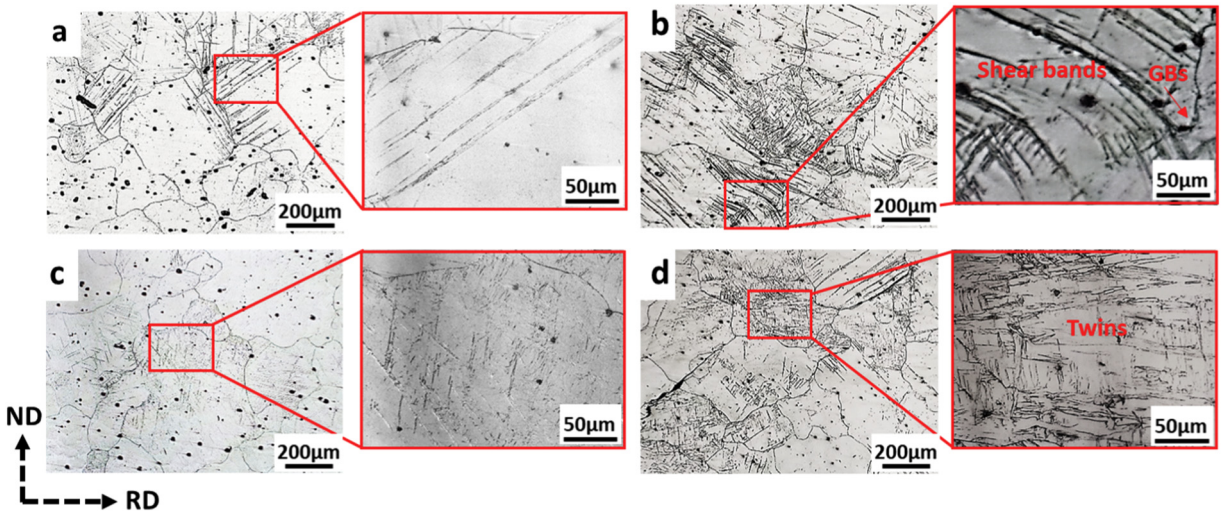


Fig. 3. Optical images and the corresponding enlarged images of the (a-b) RT-rolled and (c-d) LNT-rolled AZ31 samples. The total TRs of the samples are (a, c) 3% and (b, d) 13%.

boundaries and twin boundaries at LNT [35]. Similar results were also reported in the high strain-rate plane strain compression tests [46] and rolling tests [47].

Fig. 4 provides a detailed analysis of the twin types in the 3% RT-rolled and the 3% LNT-rolled samples. As shown in Fig. 4(a–d), three types of twins, i.e. $\{10\bar{1}2\}$ TTWs, $\{10\bar{1}1\}$-$\{10\bar{1}2\}$ DTWs and $\{10\bar{1}1\}$ CTWs, were observed in the 3% RT-rolled sample. These twins were visualised in Fig. 4(b), where the green, blue and yellow lines represent $\{10\bar{1}1\}$-$\{10\bar{1}2\}$ DTWs, $\{10\bar{1}2\}$ TTWs and $\{10\bar{1}1\}$ CTWs, respectively. According to Fig. 4 (b) and (c), it can be concluded that the black bands in Figs. 4(c) and 3(a) were $\{10\bar{1}1\}$-$\{10\bar{1}2\}$ DTWs, indicating that DTWs are the major deformation structure at the early stage of the RT-rolling process (i.e. TR = 3%). These three twin types were also identified from the peaks in the misorientation distributions in Fig. 4(d). The misorientation axes and angles of these twins were plotted in the corresponding axis distribution in Fig. 4(d), and labelled with boxes and circles in corresponding colours. According to these axis distributions, the misorientation peak at 38°, 56° and 86° all shared the $<11\bar{2}0>$ axis and corresponded to $\{10\bar{1}1\}$-$\{10\bar{1}2\}$ DTWs, $\{10\bar{1}1\}$ CTWs, and $\{10\bar{1}2\}$ TTWs, respectively.

Fig. 4(e–h) shows the analysed twinning behaviour in the 3% LNT-rolled sample. Abundant TTWs were observed in the 3% LNT-rolled sample in Fig. 4(f) and (h), confirming that the short black lines, presented in Figs. 4(g) and 3(c), were TTWs, which were the major microstructure at LNT. The 3% LNT-rolled sample had a much higher density of twins (Fig. 4(f)) than those in the 3% RT-rolled sample (Fig. 4(b)). As observed in Fig. 4(f) and (h), the main twin type in LNT-rolled sample was $\{10\bar{1}2\}$ TTWs. A small fraction of $(10\bar{1}2)$-$(01\bar{1}2)$ twin-twin interactions at 60° was also presented. The $(10\,\bar{1}\,2)$-$(01\,\bar{1}\,2)$ twin-twin interaction forms when a grain twins on both the $(10\bar{1}2)$ and $(01\bar{1}2)$ planes, and 60 $<10\bar{1}0>$ is the relationship between these two tension twin variants. Table 2 listed three different misorientation relationships between two

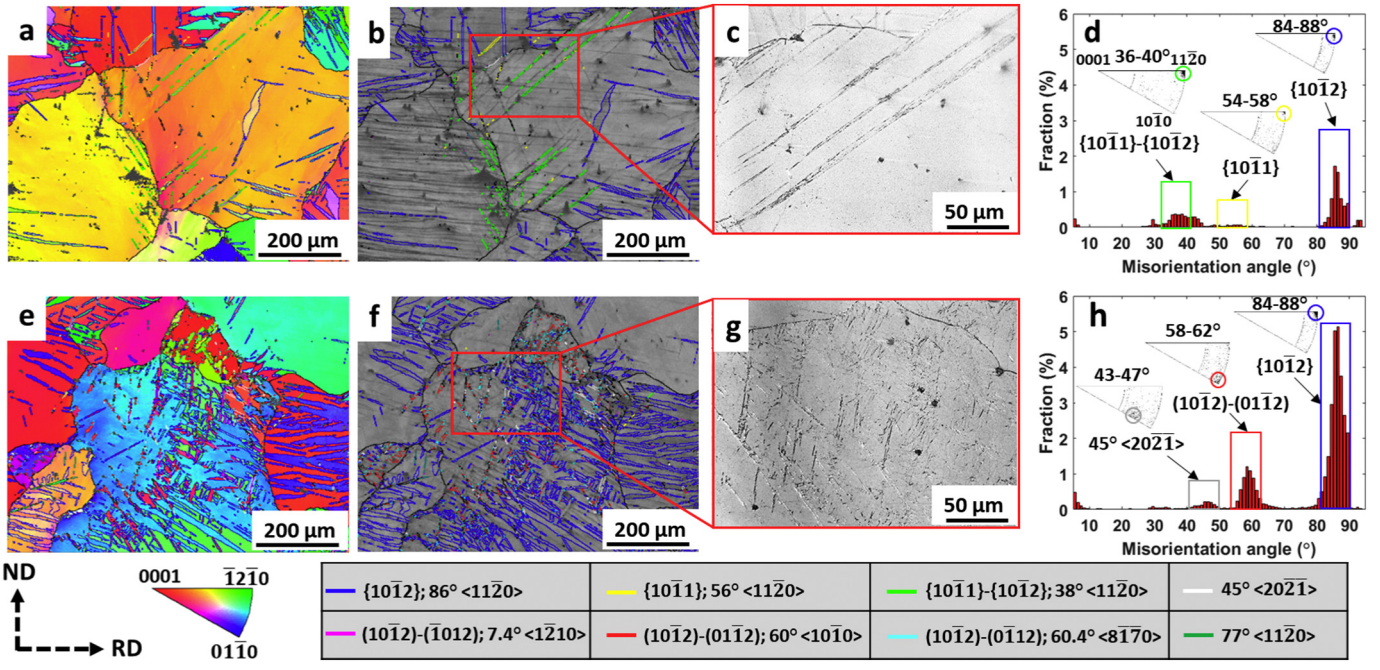


Fig. 4. EBSD analysis on the (a–d) RT-rolled and (e-h) LNT-rolled AZ31 samples with a total TR of 3%. (a) and (e) EBSD IPF images, (b) and (f) band contrast map with twin boundaries, (c) and (g) enlarged optical images, (d) and (h) misorientation distribution maps. Note that the characteristic misorientation axes and angles of the twins have been labelled using boxes and circles in (d) and (h) with the corresponding colours.

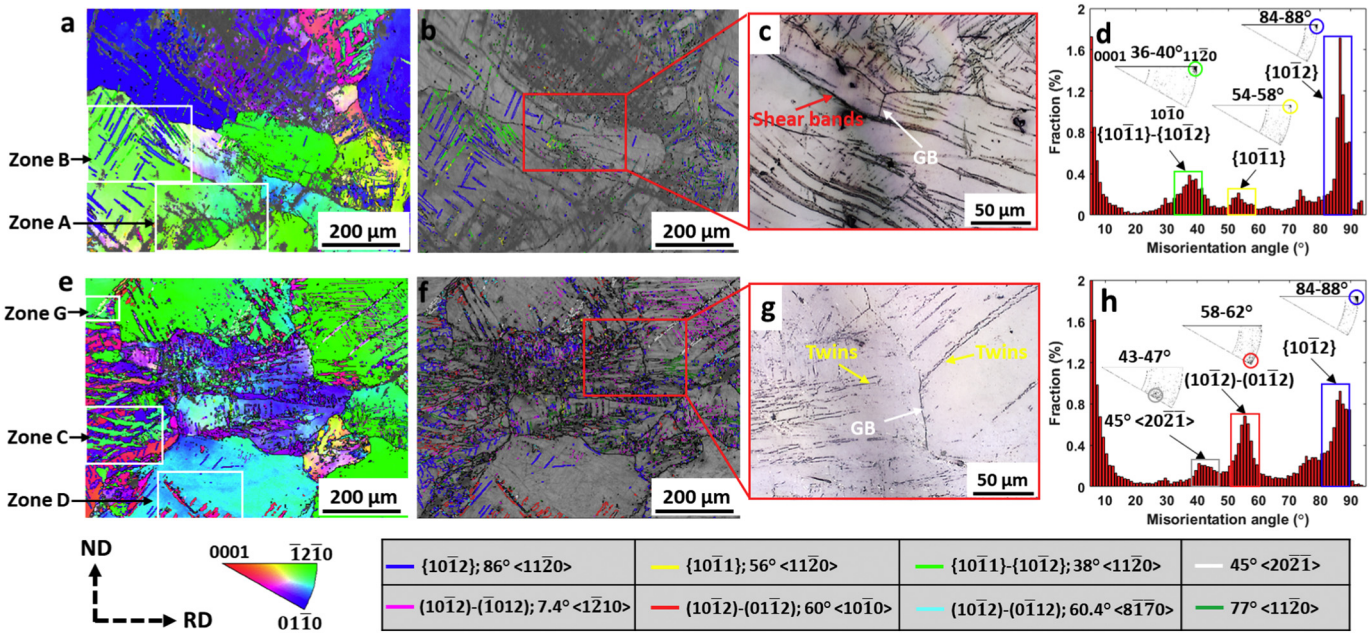


Fig. 5. EBSD analysis on the (a-d) RT-rolled and (e-h) LNT-rolled AZ31 samples with a total TR of 13%. (a) and (e) EBSD IPF images, (b) and (f) band contrast map with twin boundaries, (c) and (g) enlarged optical images, (d) and (h) misorientation distribution maps. The characteristic misorientation axes and angles of the twins have been labelled using boxes and circles in (d) and (h) with corresponding colours. (For interpretation of the references to colour in this figure legend, the reader is referred to the web version of this article.)

different tension twin variants [21]. From the axis distributions in the insets of Fig. 4(h), the peak at 86° around a <11$\bar{2}$0> axis was TTWs, and the peak at 60° around a <10$\bar{1}$0> axis was the (10$\bar{1}$2)-(01$\bar{1}$2) twin-twin interactions. However, a rarely reported peak at 45° shared a <20$\bar{2}\bar{1}$> axis, as seen in Fig. 4(h). This peak is associated with the twinning sequence, which will be analysed in detail in the following section.

EBSD analysis was also performed on the 13% RT-rolled and 13% LNT-rolled samples as shown in Fig. 5. By comparing Fig. 5 to Fig. 4,

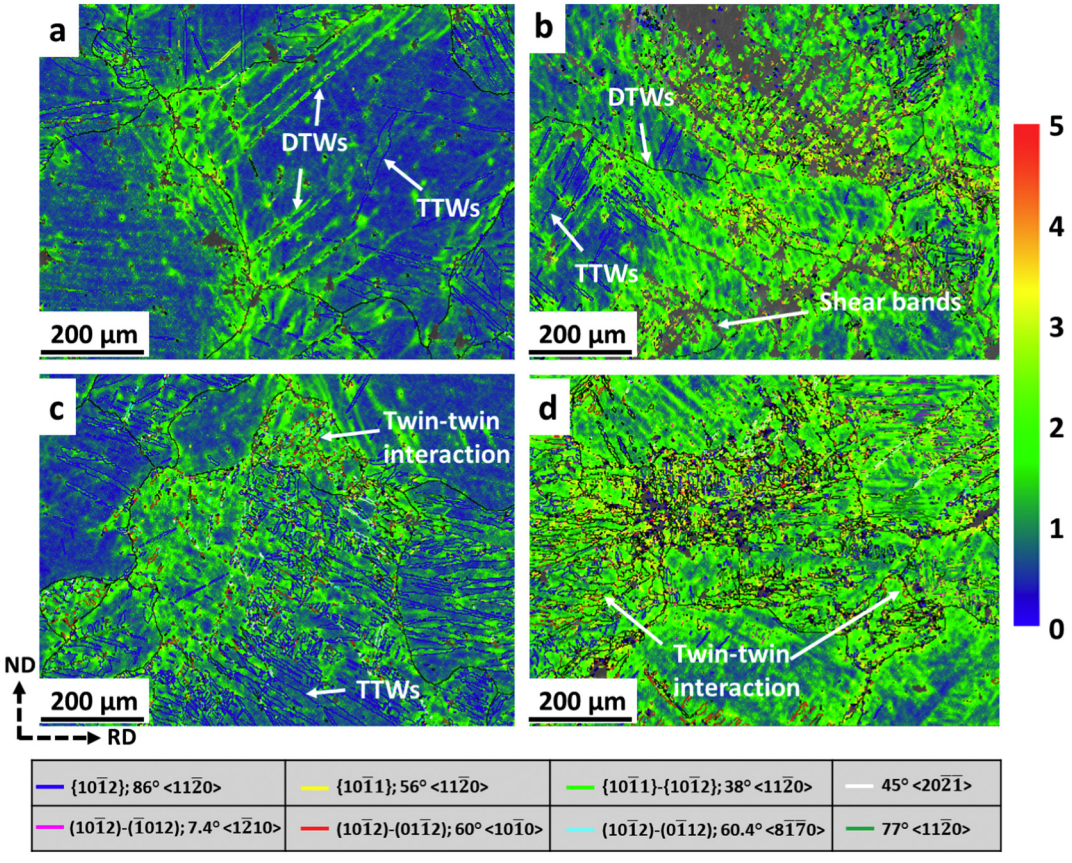


Fig. 6. KAM maps of the RT-rolled samples with a total TR of (a) 3% and (b) 13%, and of the LNT-rolled samples with a total TR of (c) 3% and (d) 13%.

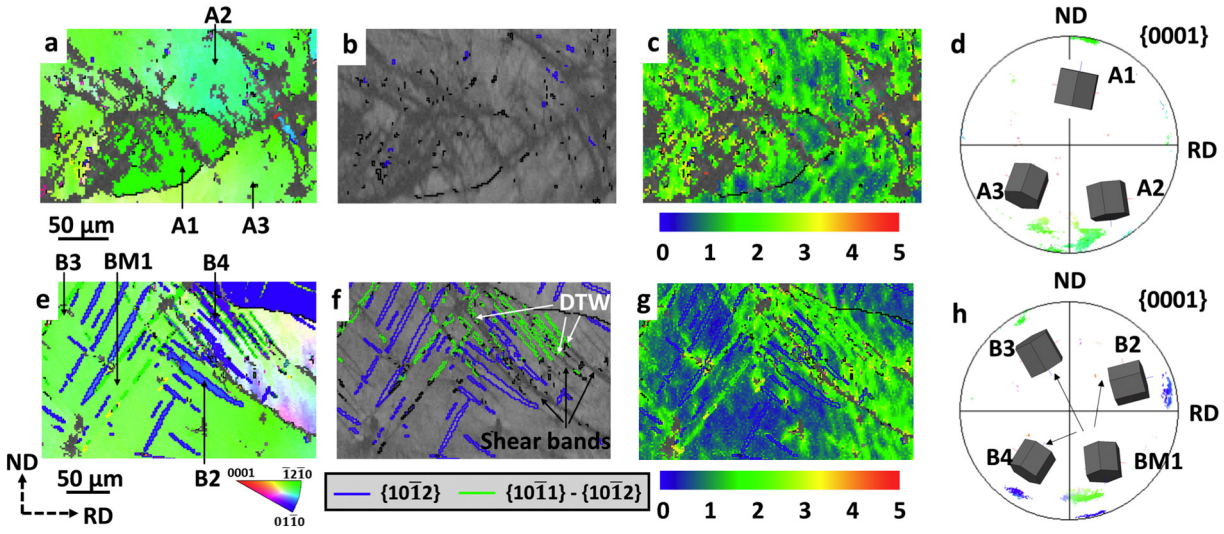


Fig. 7. Microstructures in (a–d) Zone A and (e–h) Zone B of the 13% RT-rolled sample in Fig. 5 (a). Note that the locations of Zone A and Zone B are annotated in Fig. 5 (a). (a, e) EBSD IPF images, (b, f) band contrast maps with twin boundaries, (c, g) KAM maps and (d, h) {0001} pole figures.

the insights into the evolution of twinning and shear bands can be gained. Abundant shear bands with few twins were observed in the RT-rolled samples. The grey colour represents the low band contrast (Figs. 5(b) and 7(b)), indicating the low degree of lattice perfection and high GND density in the area. This would be attributed to the intensive shear strains and deformation localization in shear bands [5,19]. Therefore, the thick lines with grey colour were identified as shear bands. This can also be confirmed by comparing the EBSD map with the optical image in Fig. 5(c), where bent and thickened lines that crossed GBs were shear bands, which were also reported in [48] under dynamic loading conditions. Considering the twin types, {10$\bar{1}$2} TTWs, {10$\bar{1}$1} CTWs and {10$\bar{1}$1}-{10$\bar{1}$2} DTWs were observed in the 13% RT-rolled sample in Fig. 5(b) and (d), which are similar to that in the 3% RT-rolled sample (Fig. 4(b)). Comparing the 3% and 13% RT-rolled samples in Figs. 4(a–d) and 5(a–d), respectively, it can be concluded that, during the RT deformation, the formation of shear bands is one of the important deformation mechanisms. Supplementary Fig. S1 plots more detailed features of the microstructures in RT-deformed samples at 3% and 13%. It is found that DTWs, as evidenced as the straight lines in Fig. S1, dominate at 3%, while shear bands, which are slightly bent and cross the grain boundaries, dominate at 13%.

Fig. 5(e–h) presents the microstructure analysis in the 13% LNT-rolled sample. More twin boundaries and fewer shear bands were observed in Fig. 5(e) and (f). Additionally, a considerable amount of {10$\bar{1}$2} TTWs and twin-twin interactions, mainly including (10$\bar{1}$2)-(01$\bar{1}$2) and (10$\bar{1}$2)-($\bar{1}$012), were identified in the 13% LNT-rolled sample, as shown in Fig. 5(f–h). Also, it is interesting to see that the 45° twin-twin misorientation around the <20$\bar{2}$1> axis are presented. Comparing the 3% and 13% LNT-rolled samples in Figs. 4(e–h) and 5(e–h), as the plastic strain increased, the major twinning types were similar, but twinning activities were more commonly seen. For example, more (10$\bar{1}$2)-(01$\bar{1}$2) twin-twin interactions and 45° <20$\bar{2}$1> twin boundaries were

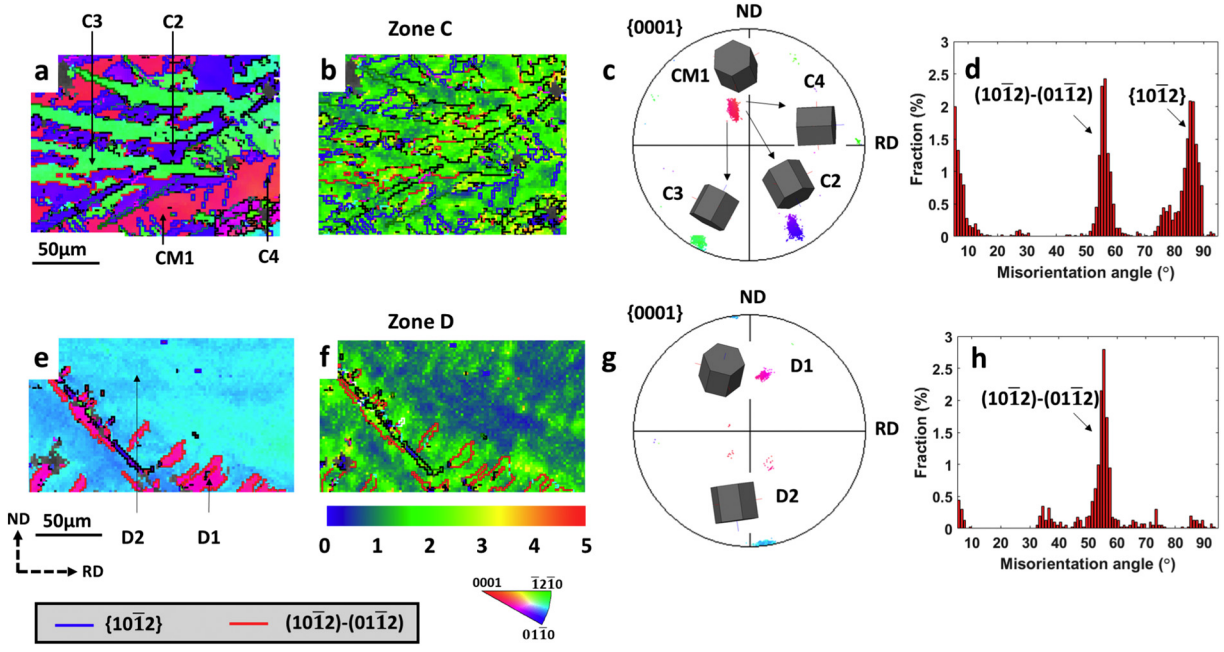


Fig. 8. Microstructures in (a–d) Zone C and (e–h) Zone D of the 13% LNT-rolled sample in Fig. 5(e). Note that the locations of Zone C and Zone D are annotated in Fig. 5(e). (a, e) EBSD IPF images, (b, f) KAM maps, (c, g) {0001} pole figures, (d, h) misorientation distribution maps.

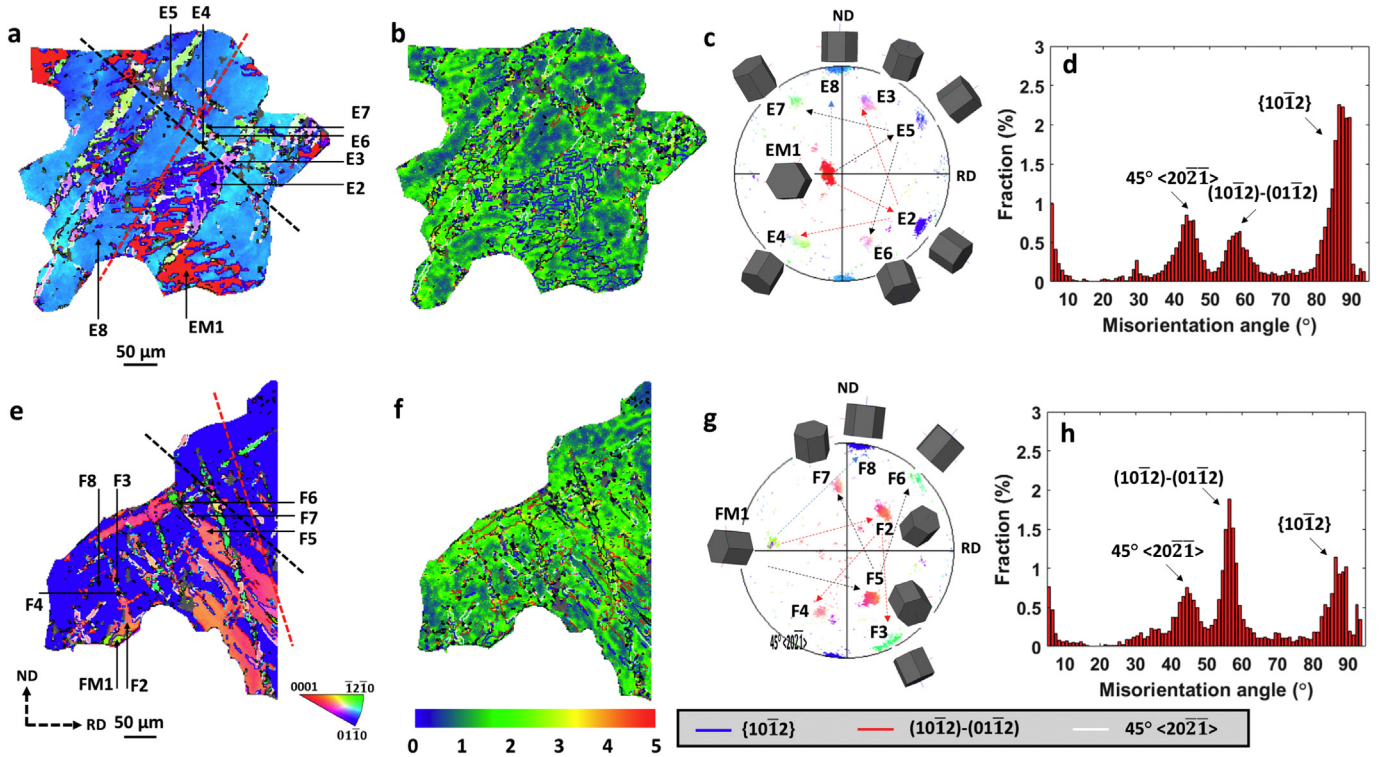


Fig. 9. Detailed microstructure analysis of (a-d) grain E and (e-h) grain F in the 9% LNT-rolled sample. (a, e) EBSD IPF images, (b, f) KAM maps, (c, g) {0001} pole figures and (d, h) misorientation distribution maps.

observed. 77° <11$\bar{2}$0> boundaries, which could be generated by the TTW, were also seen in the LNT-rolled sample, and these twin boundaries were also reported in the AZ80 alloy under dynamic impact loading [49].

The KAM maps of the RT-rolled and LNT-rolled samples with a TR of 3% and 13%, which can reflect the geometrically necessary dislocation (GND) density distributions [50,51], were summarised in Fig. 6. Generally, the KAM value progressively increased with the increase in deformation levels from 3% to 13% in both RT-rolled and LNT-rolled samples, indicating that the higher GND density was generated in a higher TR. As shown in Fig. 6(a) and (c), the GND density was low around TTWs, but was high around the DTWs and twin-twin interactions in the RT-rolled and LNT-rolled samples, respectively. For the 13% RT-rolled sample, more shear bands with high GND density were presented in Fig. 6 (b), while more twin-twin interactions with high GND density were presented in the 13% LNT-rolled sample in Fig. 6(d).

3.2. Typical zone analysis in 13% RT- and 13% LNT-rolled AZ31 samples

Four typical zones, previously annotated as Zone A, Zone B, Zone C and Zone D in Fig. 5(a) and (e), were selected and analysed in detail to further reveal the twin and shear bands distributions in RT- and LNT-rolled samples. The detailed analyses, including EBSD IPF images, band contrast, pole figure, KAM and misorientation distribution maps, are presented in Figs. 7 and 8. Zone G in Fig. 5(e) was also analysed in details and presented in Appendix III, Fig. S4.

Fig. 7(a–d) shows the microstructures in Zone A, which contained significant shear bands in the 13% RT-rolled sample. Shear bands were narrow zones of intensive shear strains and hence high KAM values. From a careful observation of Fig. 7(a–c), high KAM values were observed, especially around the shear bands, indicating that shear bands contained a wide range of internal misorientations and high GND density, as also reported in [19].

Fig. 7(e–h) presents the microstructures in Zone B, aiming to understand the relationship between twins and shear bands in the RT-rolling process. According to Fig. 7(e) and (h), twin variant B2 is {10$\bar{1}$2} TTWs, and twin variant B3 and B4 are {10$\bar{1}$1}-{10$\bar{1}$2} DTWs. As shown in Fig. 7 (e) and (f), {10$\bar{1}$2} TTWs are located outside the shear bands while {10$\bar{1}$1}-{10$\bar{1}$2} DTWs are located in the shear bands, indicating that DTWs would contribute to the shear bands formation. This is also evidenced in the corresponding KAM maps in Fig. 7(g), where the GND density is low in the {10$\bar{1}$2} TTWs, while is relatively high in the {10$\bar{1}$1}-{10$\bar{1}$2} DTWs. The high GND density in DTWs would be related to the high GND density in shear bands. Similar shear bands and twinning behaviours were also observed in the RT-rolled sample with a TR of 9%, where abundant DTWs were located along the shear bands with high GND density in Supplementary Figs. S2 (a–c) and S3 (a–b), confirming that DTWs are the major contributors to the shear bands formation.

Compared to the RT-rolled sample, the major deformation structure in the LNT-rolled sample is twinning. There are abundant (10$\bar{1}$2)-(01$\bar{1}$2) twin-twin interactions observed in the 13% LNT-rolled sample. Fig. 8(a–d) gives a detailed microstructure analysis in Zone C from Fig. 5(e). The

Table 2
Misorientations generated between different {10$\bar{1}$2} twin variants [21]

Type of twin	Misorientation angle/axis
(10$\bar{1}$2)-($\bar{1}$012)	7.4° <1$\bar{2}$10>
(10$\bar{1}$2)-(01$\bar{1}$2)	60.0° <10$\bar{1}$0>
(10$\bar{1}$2)-(0$\bar{1}$12)	60.4° <8$\bar{1}$70>

main twin types in Zone C were {10$\bar{1}$2} TTWs and (10$\bar{1}$2)-(01$\bar{1}$2) twin-twin interactions. As shown in Fig. 8(a), three tension twin variants, i.e. C2, C3 and C4, were generated from the parent matrix CM1 and the misorientations between the matrix and these twin variants were ~86°, as identified in Fig. 8(c) and (d). The (10$\bar{1}$2)-(01$\bar{1}$2) twin-twin interactions were generated between twin variant C2 and C3. A 60° <10$\bar{1}$0> misorientation between twin variant C2 and C3 was observed in Fig. 8(c) and (d). Fig. 8(b) presents the KAM map, where high GND density was observed around the boundaries of the twin-twin interactions.

Fig. 8(e–h) illustrates the analysis of the microstructure in Zone D of the 13% LNT-rolled sample. The analysis of Zone D is used to clearly show the (10$\bar{1}$2)-(01$\bar{1}$2) twin-twin interaction. As shown in Fig. 8(e), (g) and (h), the (10$\bar{1}$2)-(01$\bar{1}$2) twin-twin interaction was observed between twin variant D1 with D2. The misorientation between twin variant D1 and D2 was approximately 60° around an <10$\bar{1}$0> axis, where an apparent single peak was observed in Fig. 8(h). The matrix was almost consumed by these two twin variants. This indicates that twinning is an effective means to accommodate plastic deformation in the LNT condition. Also, the twin-twin interaction is an effective dislocation barrier as demonstrated by the high KAM values, in Fig. 8(f).

3.3. Twinning sequence analysis

In the LNT-rolled sample, a new twinning sequence is found. Primary TTWs formed first and, subsequently, a set of secondary TTWs formed within them. To thoroughly study this twinning behaviour, two single grains, namely grain E and F, were taken from the 9% LNT-rolled sample, and analysed in details in Fig. 9. For clarity, the full EBSD maps of the 9% LNT-rolled sample are presented in Supplementary Figs. S2 and S3.

Fig. 9(a–d) presents the analysis of grain E. It is difficult to use the captured EBSD map to distinguish the matrix with the twin variant and the sequence of the twin variants. Hence, the most possible twinning behaviours were described in this work, based on the misorientation and axes of the typical twins. Fig. 9(a) and (c) plot the IPF map and the corresponding orientations of matrix and twin variants in the {0001} pole figure. Three primary tension twin variants E2, E5 and E8 were generated from the matrix EM1, as observed in Fig. 9(a) and (c). The primary tension twin variants, E2, E5 and E8 interacted and formed the (10$\bar{1}$2)-(01$\bar{1}$2) twin-twin interactions. The tension twin variant E8 consumed the majority of the matrix EM1, and no secondary twin was generated in twin variant E8. However, secondary tension twin variants, E3 and E4, were generated from primary twin variant E2. The two secondary tension twin variants, E3 and E4, also formed the secondary (10$\bar{1}$2)-(01$\bar{1}$2) twin-twin interactions. It is worth noting that the primary twin variant E2 and secondary twin variants E3 and E4 were distributed along a line which was parallel to the red dotted line in Fig. 9 (a). Secondary tension twin variants E6 and E7 were also generated from primary twin variant E5 and formed the secondary (10$\bar{1}$2)-(01$\bar{1}$2) twin-twin interactions. These twin variants, E5, E6 and E7, were distributed along a line which was parallel to the black dotted line in Fig. 9 (a). Therefore, a new twinning sequence of primary TTW-TTW interaction → secondary TTW-TTW interaction can be established. This special twinning sequence would result from the suppression of dislocation slips, in order to accommodate the plastic strain at cryogenic temperature.

The secondary twin variants, i.e. E3, E4, E6 and E7, interacted with the primary twin variant E8 to generate a special ~45° misorientation around an <20$\bar{2}$1> axis (45° <20$\bar{2}$1>). As shown in Fig. 9(c), in addition to the misorientation peak of 86° {10$\bar{1}$2} TTWs and 60° (10$\bar{1}$2)-(01$\bar{1}$2) twin-twin interaction, a ~45° misorientation peak was observed, resulting from the interactions between the secondary and the primary twin variants. Fig. 9(b) presents the KAM distributions around these twin-twin interactions. High KAM values were observed around the interactions, indicating that the boundaries of these twin-twin interactions would block the dislocation slips and result in high GND density. In addition, the twinning sequence would result in twinning-induced grain refinement.

Fig. 9(e–h) provides a similar microstructure analysis on grain F to confirm this twinning structure. As shown in Fig. 9(e–f), a similar twinning sequence was observed. The primary tension twin variants F2, F5, F8 were generated from the matrix FM1. Although the volume fraction of F8 is high, F8 is more likely to be a twin variant. As the c-axis of F8 is almost parallel to ND and the compression direction in the pole figure, it would be more difficult to activate the TTWs in this orientation of F8 than FM1, where its c-axis is almost perpendicular to the compression direction [52]. It is also reasonable to observe the high volume fraction of F8, because TTWs can form a profuse structure and consume the majority of the parent structure at 9% deformation [53]. The primary twin variant F2 and F5 interacted with the twin variant F8 to form 60° <10$\bar{1}$0> boundaries, namely (10$\bar{1}$2)-(01$\bar{1}$2) twin-twin interactions. The secondary tension twin variants F3 and F4 were generated from the primary twin variant F2, and these three twin variants were distributed parallel to the red dotted line in Fig. 9(e). These two secondary tension twin variants F3 and F4 interacted and formed the secondary (10$\bar{1}$2)-(01$\bar{1}$2) twin-twin interaction. The secondary twin variants F6, F7 and primary twin variant F5 also showed the similar relationship to the secondary twin variants F3, F4 and primary twin variant F2, but the twin variants F5, F6 and F7 were distributed parallel to the black dotted line in Fig. 9(e). According to Fig. 9(e) and (g), the secondary tension twin variants F3, F4, F6 and F7 interacted with the primary tension twin variant F8 to form 45° <20$\bar{2}$1> boundaries. Three misorientation distribution peaks, including 86°{10$\bar{1}$2} TTWs, 60° (10$\bar{1}$2)-(01$\bar{1}$2) twin-twin interactions, and 45° <20$\bar{2}$1> boundaries were observed in Fig. 9(h). As shown in Fig. 9(f), higher GND density was observed around boundaries of these twin-twin interactions, compared to other areas in grain F, indicating that these boundaries of twin-twin interactions would block and accumulate GNDs easily. The detailed analysis of grain E and F concluded that there was a special twinning sequence behaviour in the LNT-rolled sample, where secondary TTWs formed on the primary TTWs and interacted with another set of primary TTWs to form 45° <20$\bar{2}$1> boundaries. The detailed analysis of the grain E and F confirmed the occurrence of the specific twinning sequence and twin-twin interactions in the LNT-rolled sample, additionally, thoroughly explained the configurations of the lattice orientations.

4. Discussion

4.1. Illustration of microstructure evolution during RT-rolling and LNT-rolling process

An integrated schematic illustration of the microstructure evolutions during the RT- and LNT-rolling process with respect to deformation levels was presented in Fig. 10. At the early stage of the RT-rolling (from Fig. 10 (a) to (b)), some {10$\bar{1}$1}-{10$\bar{1}$2} DTWs, few TTWs and shear bands were generated. With the increase in the deformation levels (from Fig. 10(b) to (c)), more shear bands were generated, which were transformed from the existing DTWs, to accommodate the plastic deformation. A small amount of TTWs and DTWs were still left in the matrix. Abundant GNDs were observed in the RT-rolled sample and accumulated around the shear bands and DTWs (Figs. 6–7 and 10).

During the LNT-rolling process, the main deformation structures are twins, including TTWs, twin-twin interactions and twinning sequence. At the initial deformation stage, a significant amount of thin and individual twins, especially the TTWs, were generated in the LNT-rolled sample, as shown in Fig. 4(e–h), Fig. 10(d) and (e). With the increase in deformation levels, unlike the RT-rolled sample, where DTWs are

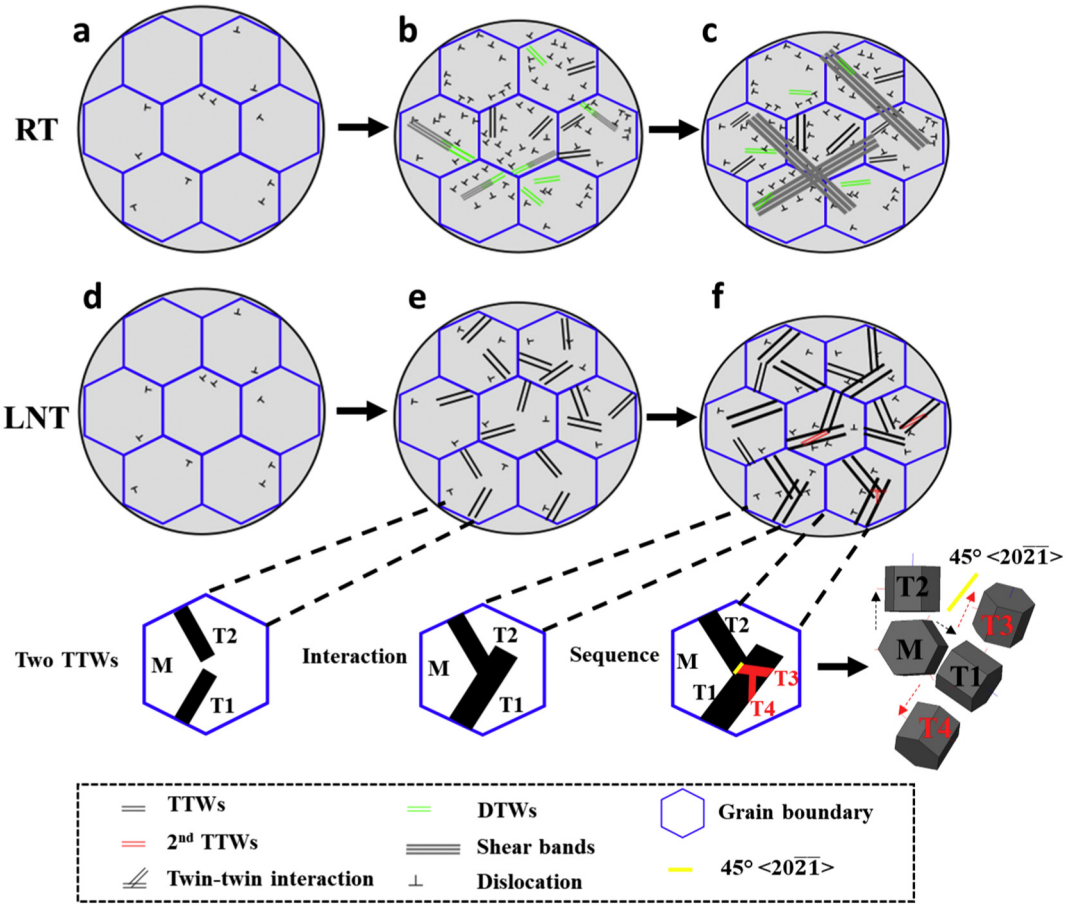


Fig. 10. Schematic illustration of the *microstructure evolution* during (a–c) RT and (d–f) LNT-rolling process. Insets plot the formation process of twin-twin interactions and twinning sequence.

transformed into shear bands, active twin behaviours occur to accommodate further plastic strains during the LNT-rolling process. As shown in Figs. 5(e–h) and 10(f), the TTWs were interacted to form $(10\bar{1}2)$-$(01\bar{1}2)$ twin-twin interactions. Additionally, the secondary TTWs were generated from the primary TTWs to form $\{10\bar{1}2\}$-$\{10\bar{1}2\}$ double tension twins, which is the so-called twinning sequence. More importantly, the secondary twin-twin interaction in primary twin-twin interaction was observed for the first time, creating a specific misorientation of ~45° between the primary TTW variant and another secondary TTW variant, as shown in Figs. 9 and 10(f). The detailed twinning behaviours including twinning sequence are shown in the insets below. Primary twin variants T1 and T2 form the twin-twin interaction, and then the secondary twin variant T3 in the primary twin variant T1 would meet with another primary twin variant T2 to form the specific boundaries, namely 45° <20$\bar{2}$1> boundaries. GND accumulations are mainly located around the boundaries of twin-twin interactions and twinning sequence in the LNT-rolled sample, according to Figs. 6–10.

4.2. Twinning behaviours during LNT-rolling process

The active twinning behaviours during LNT-rolling process would be attributed to the limited dislocation slips to accommodate the strain at LNT. It is well-known that the temperature almost has no effect on the CRSS for twinning, but the CRSS for dislocation slip stress increases with decreasing temperature [39,54]. Hence the dislocation slip would be suppressed at a lower temperature while twinning becomes more active. Fewer slip activities reduced the ability to relieve the strain misfit between the neighbour grains at a lower temperature, resulting in low deformation compatibility and hence high local stress near GBs in the LNT-rolled sample [35]. Twin nucleation commonly requires the large stress or stress concentration [55–57], for example, grain boundaries in which stress concentrations and source defects are located [58,59]. Therefore, active twinning behaviours are expected in the LNT-rolled sample, due to limited dislocation slips and high local stress near boundaries.

The formation of abundant TTWs and twin-twin interactions at LNT could result from the significant local stress in the cryogenic deformation. Abundant twins were also reported in cryo-rolling of titanium, it is speculated that it is easier to activate the twin nucleation at cryogenic temperature, compared to at RT, which would be attributed to the significant local stress concentrations near GBs [35]. Therefore, significant local stress in the LNT-rolled sample would trigger the formation of abundant TTWs. These twins would grow and interact with each other to form twin-twin interactions [21,26,28].

The rare $\{10\bar{1}2\}$-$\{10\bar{1}2\}$ double tension twins were also observed during the LNT-rolling process, and the twins are different from $\{10\bar{1}1\}$-$\{10\bar{1}2\}$ DTWs, which were commonly observed in the deformation process at RT [29,30]. $\{10\bar{1}2\}$-$\{10\bar{1}2\}$ double tension twins were generally observed in multiaxial stress fields [31,34] or low temperature [42]. The reason for the formation of the unusual $\{10\bar{1}2\}$-$\{10\bar{1}2\}$ double tension twins could also be attributed to the high local stress. It was proposed that the formation of $\{10\bar{1}2\}$-$\{10\bar{1}2\}$ double tension twins were caused by difficult non-basal slips at low temperatures [42], which could result in stress concentrations, as no sufficient dislocation slips are effectively generated to relieve the local stresses. In addition, the twin transformations, such as ~13%

shear induced by TTWs, could induce local stress near the twins [60], and the high local stress near TTWs would provide the stress for the nucleation of secondary TTWs.

Regarding the formation of the special twinning sequence, i.e. the secondary twin-twin interaction in the primary twin-twin interaction, it could be attributed to the following reasons. (i) The primary twin-twin interaction would generate high local stress around the boundaries [25], which could promote secondary twin nucleations. (ii) At lower temperatures, as the required stress for dislocation slip is higher, more secondary twins are generated to accommodate the further plastic strain. Finally, these secondary twins would grow and meet to form the secondary twin-twin interactions in the primary twin-twin interactions.

GND density accumulations were observed around the boundaries of twin-twin interactions and twinning sequence. Some dislocation slips are activated at LNT, demonstrated indirectly by the KAM maps. However, the dislocation density at LNT is expected to be lower than RT, due to the increasing CRSS for dislocation slips with decreasing temperature [35,36]. This would be attributed to the following reasons. Firstly, the structures of twin-twin interactions and twinning sequence are generally fine, so the dislocation slips will be blocked effectively by their twin boundaries, according to the boundary hardening effects [61]. Secondly, the twin variants would show different orientations and provide various paths for dislocation slips, resulting in abundant dislocation accumulations. In addition, twin-twin boundaries in twin-twin interactions would react to form boundary dislocations [26,27].

4.3. Shear bands formation during RT-rolling process

According to Figs. 3, 5–7, and Supplementary Fig. S1, the bent bands in 13% RT-rolled sample pass through the grain boundaries, contain shear layers and accumulate abundant GNDs. These phenomena are the typical features in shear bands and a result of the plastic instability, confirming that these bands in 13% RT-rolled sample are shear bands [9].

Shear bands formation in magnesium alloys generally results from the evolvement of twinning and dynamic recrystallisation. As these rolling tests were conducted at room and liquid nitrogen temperature, recrystallisation phenomenon was not expected. Therefore, the formation of shear bands would be mainly related to the deformation twins. As shown in Figs. 4(a–d) and 7, the main microstructures in the RT-rolled sample with a TR of 3% are $\{10\bar{1}2\}$ TTWs, $\{10\bar{1}1\}$-$\{10\bar{1}2\}$ DTWs and $\{10\bar{1}1\}$ CTWs. In Figs. 5(a–d) and 7, with TR increasing to 13%, abundant shear bands were generated in the RT-rolled AZ31 sample, and some $\{10\bar{1}1\}$-$\{10\bar{1}2\}$ DTWs and $\{10\bar{1}1\}$ CTWs were observed. Only DTWs were located within the shear bands with high GND density, indicating that these DTWs accommodated the large plastic strain and could contribute to the formation of shear bands.

DTWs in shear bands provide a favoured path for basal slips, and substantial dislocation slips would pile up around these twin boundaries, resulting in stress concentration and distortion of these twin boundaries (Fig. 7(g)). The GND density was generally high inside shear bands, which could be related to the high GND density in DTWs, as observed in Fig. 7(c) and (g) and also in [62]. In addition, the basal plane in DTWs is reoriented to be well oriented for slips, this could also result in crystallographic softening in these twins [30]. Therefore, these phenomena in DTWs are strongly linked to the shear bands where abundant dislocation slips and softening occur, confirming that the shear bands are originated from DTWs in the RT-rolled sample. This result is in good agreement with some research on the formation of shear bands [5–7], for example, the shear bands developed from $\{10\bar{1}1\}$-$\{10\bar{1}2\}$ DTWs in compression tests of Mg alloys sheets [15].

TTWs were located outside these shear bands with low GND density in Fig. 7(f) and (g), indicating that TTWs may not play an important role in the formation of shear bands. TTWs were generally unfavourably oriented for basal slips, while basal slips were frequently observed in DTWs [3]. Hence higher GND density is expected around DTWs compared to TTWs. It is found that basal slip can be easily transmitted through TTWs boundaries [63], so the dislocation pile-ups along TTWs boundaries could be low, resulting in difficulty in accumulating GNDs around these boundaries and contributing to the shear bands formation.

5. Conclusions

In this study, a detailed microstructure analysis was performed on the RT- and LNT-rolled AZ31 magnesium alloys. The deformation structures at RT and LNT were examined, delivering comprehensive understandings of the evolved deformation twins, shear bands, GNDs and their dynamic interactions. More importantly, a rarely observed twinning sequence formed at LNT to accommodate the plastic deformation. The following conclusions were made:

(i) A new deformation behaviour (i.e. twinning sequence): primary TTW-TTW interactions → secondary TTW-TTW interactions, with a 45° <$20\bar{2}1$> misorientation peak, was discovered in the LNT-rolling process. This 45° <$20\bar{2}\bar{1}$> misorientation peak was created between the secondary and another primary tension twin variant.

(ii) The major deformation structure during the RT-rolling process was identified as $\{10\bar{1}1\}$-$\{10\bar{1}2\}$ DTWs → shear bands, during which high GND density accumulated around DTWs and contributed to the formation of shear bands.

(iii) Abundant twins, starting from $\{10\bar{1}2\}$ TTWs to twin-twin interactions and twinning sequence, were observed during the LNT-rolling process. These active twinning behaviours would mainly result from the limited dislocation slips and high local stress at LNT.

(iv) The boundaries of twin-twin interactions and twinning sequence are the preferential sites for high GND density accumulations, while the GND density is low in TTWs.

CRediT authorship contribution statement

Kai Zhang: Conceptualization, Data curation, Formal analysis, Investigation, Methodology, Software, Validation, Visualization, Writing - original draft, Writing - review & editing.**Jing-Hua Zheng:**Supervision, Investigation, Visualization, Conceptualization, Writing - original draft, Writing - review & editing.**Yan Huang:**Investigation, Visualization, Writing - review & editing.**Catalin Pruncu:**Investigation, Visualization, Writing - review & editing.**Jun Jiang:**Supervision, Conceptualization, Funding acquisition, Resources, Investigation, Visualization, Writing - original draft, Writing - review & editing.

Declaration of competing interest

The authors declare that they have no known competing financial interests or personal relationships that could have appeared to influence the work reported in this paper.

Acknowledgements

We are grateful for the financial support from the President's PhD Scholarship of Imperial College London. The authors would like to thank the funding support by EPSRC under the Grant Agreement EP/R001715/1 on "LightForm: Embedding Materials Engineering in Manufacturing with Light Alloys".

Appendix A. Supplementary data

Supplementary data to this article can be found online at https://doi.org/10.1016/j.matdes.2020.108793.

References

[1] F. Zarandi, S. Yue, Magnesium sheet; challenges and opportunities, Magnesium Alloys-Design, Processing and Properties, InTech, 2011.
[2] H. Pan, Y. Ren, H. Fu, H. Zhao, L. Wang, X. Meng, G. Qin, Recent developments in rare-earth free wrought magnesium alloys having high strength: a review, J. Alloys Compd. 663 (2016) 321–331.
[3] D. Guan, W.M. Rainforth, J. Gao, J. Sharp, B. Wynne, L. Ma, Individual effect of recrystallisation nucleation sites on texture weakening in a magnesium alloy: part 1- double twins, Acta Mater. 135 (2017) 14–24.
[4] K. Zhang, J.-H. Zheng, Z. Shao, C. Pruncu, M. Turski, C. Guerini, J. Jiang, Experimental investigation of the viscoplastic behaviours and microstructure evolutions of AZ31B and Elektron 717 mg-alloys, Mater. Des. 184 (2019).
[5] M.R. Barnett, M.D. Nave, C.J. Bettles, Deformation microstructures and textures of some cold rolled Mg alloys, Mater. Sci. Eng. A 386 (1–2) (2004) 205–211.
[6] P. Changizian, A. Zarei-Hanzaki, M. Ghambari, A. Imandoust, Flow localization during severe plastic deformation of AZ81 magnesium alloy: micro-shear banding phenomenon, Mater. Sci. Eng. A 582 (2013) 8–14.
[7] K. Atik, M. Efe, Twinning-induced shear banding and its control in rolling of magnesium, Mater. Sci. Eng. A 725 (2018) 267–273.
[8] C. Xie, Q.H. Fang, X. Liu, P.C. Guo, J.K. Chen, M.H. Zhang, Y.W. Liu, B. Rolfe, L.X. Li, Theoretical study on the{1¯012}deformation twinning and cracking in coarse-grained magnesium alloys, Int. J. Plast. 82 (2016) 44–61.
[9] F.J. Humphreys, M. Hatherly, Recrystallization and Related Annealing Phenomena, Elsevier, 2012.
[10] S.V. Harren, H.E. Dève, R.J. Asaro, Shear band formation in plane strain compression, Acta Metall. 36 (9) (1988) 2435–2480.
[11] J.R. Rice, Localization of Plastic Deformation, Brown Univ, Providence, RI (USA), 1976 Div. of Engineering.
[12] İ.B. Üçel, E. Kapan, O. Türkoğlu, C.C. Aydıner, In situ investigation of strain heterogeneity and microstructural shear bands in rolled magnesium AZ31, Int. J. Plast. 118 (2019) 233–251.
[13] G.D. Köhlhoff, A.S. Malin, K. Lücke, M. Hatherly, Microstructure and texture of rolled {112}⟨111⟩ copper single crystals, Acta Metall. 36 (10) (1988) 2841–2847.
[14] W. Österle, H. Wever, H.J. Bunge, Development of microstructure and texture of cold rolled α iron, Metal Science 17 (7) (1983) 333–340.
[15] H.L. Kim, J.H. Lee, C.S. Lee, W. Bang, S.H. Ahn, Y.W. Chang, Shear band formation during hot compression of AZ31 Mg alloy sheets, Mater. Sci. Eng. A 558 (2012) 431–438.
[16] S.E. Ion, F.J. Humphreys, S.H. White, Dynamic recrystallisation and the development of microstructure during the high temperature deformation of magnesium, Acta Metall. 30 (10) (1982) 1909–1919.
[17] Y. Wang, Y. Xin, H. Yu, L. Lv, Q. Liu, Formation and microstructure of shear bands during hot rolling of a Mg–6Zn–0.5Zr alloy plate with a basal texture, J. Alloys Compd. 644 (2015) 147–154.
[18] Y.B. Chun, C.H.J. Davies, Texture effects on development of shear bands in rolled AZ31 alloy, Mater. Sci. Eng. A 556 (2012) 253–259.
[19] D. Guan, W.M. Rainforth, J. Gao, L. Ma, B. Wynne, Individual effect of recrystallisation nucleation sites on texture weakening in a magnesium alloy: part 2- shear bands, Acta Mater. 145 (2018) 399–412.
[20] S.-G. Hong, S.H. Park, C.S. Lee, Role of {10−12} twinning characteristics in the deformation behavior of a polycrystalline magnesium alloy, Acta Mater. 58 (18) (2010) 5873–5885.
[21] M.D. Nave, M.R. Barnett, Microstructures and textures of pure magnesium deformed in plane-strain compression, Scr. Mater. 51 (9) (2004) 881–885.
[22] A. Staroselsky, L. Anand, A constitutive model for hcp materials deforming by slip and twinning, Int. J. Plast. 19 (10) (2003) 1843–1864.
[23] C.M. Cepeda-Jiménez, J.M. Molina-Aldareguia, M.T. Pérez-Prado, Origin of the twinning to slip transition with grain size refinement, with decreasing strain rate and with increasing temperature in magnesium, Acta Mater. 88 (2015) 232–244.
[24] A. Chapuis, J.H. Driver, Temperature dependency of slip and twinning in plane strain compressed magnesium single crystals, Acta Mater. 59 (5) (2011) 1986–1994.
[25] M. Arul Kumar, M. Gong, I.J. Beyerlein, J. Wang, C.N. Tomé, Role of local stresses on co-zone twin-twin junction formation in HCP magnesium, Acta Mater. 168 (2019) 353–361.
[26] Q. Yu, J. Wang, Y. Jiang, R.J. McCabe, N. Li, C.N. Tomé, Twin–twin interactions in magnesium, Acta Mater. 77 (2014) 28–42.
[27] M. Gong, S. Xu, Y. Jiang, Y. Liu, J. Wang, Structural characteristics of {1¯012} non-cozone twin-twin interactions in magnesium, Acta Mater. 159 (2018) 65–76.
[28] H. El Kadiri, J. Kapil, A.L. Oppedal, L.G. Hector, S.R. Agnew, M. Cherkaoui, S.C. Vogel, The effect of twin–twin interactions on the nucleation and propagation of twinning in magnesium, Acta Mater. 61 (10) (2013) 3549–3563.
[29] M. Lentz, M. Risse, N. Schaefer, W. Reimers, I.J. Beyerlein, Strength and ductility with {1011} - {1012} double twinning in a magnesium alloy, Nat. Commun. 7 (2016) 11068.
[30] M.R. Barnett, Twinning and the ductility of magnesium alloys part II. “Contraction” twins, Mater. Sci. Eng. A 464 (1–2) (2007) 8–16.
[31] Z.-Z. Shi, Y. Zhang, F. Wagner, T. Richeton, P.-A. Juan, J.-S. Lecomte, L. Capolungo, S. Berbenni, Sequential double extension twinning in a magnesium alloy: combined statistical and micromechanical analyses, Acta Mater. 96 (2015) 333–343.
[32] S. Hyuk Park, S.-G. Hong, C.S. Lee, In-plane anisotropic deformation behavior of rolled Mg–3Al–1Zn alloy by initial {10–12} twins, Mater. Sci. Eng. A 570 (2013) 149–163.
[33] S.H. Park, S.-G. Hong, J.H. Lee, C.S. Lee, Multiple twinning modes in rolled Mg–3Al–1Zn alloy and their selection mechanism, Mater. Sci. Eng. A 532 (2012) 401–406.
[34] A. Jäger, A. Ostapovets, P. Molnár, P. Lejček, { }-{ } double twinning in magnesium, Philos. Mag. Lett. 91 (8) (2011) 537–544.
[35] S.-W. Choi, J.W. Won, S. Lee, J.K. Hong, Y.S. Choi, Deformation twinning activity and twin structure development of pure titanium at cryogenic temperature, Mater. Sci. Eng. A 738 (2018) 75–80.
[36] M.A. Meyers, O. Vöhringer, V.A. Lubarda, The onset of twinning in metals: a constitutive description, Acta Mater. 49 (19) (2001) 4025–4039.
[37] A. Jain, S.R. Agnew, Modeling the temperature dependent effect of twinning on the behavior of magnesium alloy AZ31B sheet, Mater. Sci. Eng. A 462 (1–2) (2007) 29–36.
[38] S.R. Agnew, Ö. Duygulu, Plastic anisotropy and the role of non-basal slip in magnesium alloy AZ31B, Int. J. Plast. 21 (6) (2005) 1161–1193.
[39] S.V. Zherebtsov, G.S. Dyakonov, A.A. Salem, V.I. Sokolenko, G.A. Salishchev, S.L. Semiatin, Formation of nanostructures in commercial-purity titanium via cryorolling, Acta Mater. 61 (4) (2013) 1167–1178.
[40] F. Kabirian, A.S. Khan, T. Gnäupel-Herlod, Visco-plastic modeling of mechanical responses and texture evolution in extruded AZ31 magnesium alloy for various loading conditions, Int. J. Plast. 68 (2015) 1–20.
[41] A. Kula, X. Jia, R.K. Mishra, M. Niewczas, Flow stress and work hardening of Mg-Y alloys, Int. J. Plast. 92 (2017) 96–121.
[42] J. Jain, J. Zou, C.W. Sinclair, W.J. Poole, Double tensile twinning in a Mg-8Al-0.5Zn alloy, J. Microsc. 242 (1) (2011) 26–36.
[43] J. Luo, Y. Yan, J. Zhang, L. Zhuang, Microstructure and mechanical properties of a basal textured AZ31 magnesium alloy cryorolled at liquid-nitrogen temperature, Met. Mater. Int. 22 (4) (2016) 637–641.
[44] M. Calcagnotto, D. Ponge, E. Demir, D. Raabe, Orientation gradients and geometrically necessary dislocations in ultrafine grained dual-phase steels studied by 2D and 3D EBSD, Mater. Sci. Eng. A 527 (10−11) (2010) 2738–2746.
[45] L.E. Samuels, Metallographic Polishing by Mechanical Methods, Asm International, 2003.
[46] X. Liu, B.W. Zhu, C. Xie, J. Zhang, C.P. Tang, Y.Q. Chen, Twinning, dynamic recrystallization, and crack in AZ31 magnesium alloy during high strain rate plane strain compression across a wide temperature, Mater. Sci. Eng. A 733 (2018) 98–107.
[47] B. Zhu, X. Liu, C. Xie, J. Su, P. Guo, C. Tang, W. Liu, Unveiling the underlying mechanism of forming edge cracks upon high strain-rate rolling of magnesium alloy, J. Mater. Sci. Technol. 50 (2020) 59–65.
[48] P. Guo, L. Li, X. Liu, T. Ye, S. Cao, C. Xu, S. Li, Compressive deformation behavior and microstructure evolution of AM80 magnesium alloy under quasi-static and dynamic loading, Int. J. Impact Eng. 109 (2017) 112–120.
[49] L. Mao, C. Liu, T. Chen, Y. Gao, S. Jiang, R. Wang, Twinning behavior in a rolled Mg-Al-Zn alloy under dynamic impact loading, Scr. Mater. 150 (2018) 87–91.
[50] C.K. Yan, A.H. Feng, S.J. Qu, G.J. Cao, J.L. Sun, J. Shen, D.L. Chen, Dynamic recrystallization of titanium: effect of pre-activated twinning at cryogenic temperature, Acta Mater. 154 (2018) 311–324.
[51] D.-X. Wei, Y. Koizumi, M. Nagasako, A. Chiba, Refinement of lamellar structures in Ti-Al alloy, Acta Mater. 125 (2017) 81–97.
[52] T.B. Britton, F.P.E. Dunne, A.J. Wilkinson, On the mechanistic basis of deformation at the microscale in hexagonal close-packed metals, Proc. R. Soc. A: Mathematical, Physical and Engineering Science 471 (2178) (2015).
[53] H. El Kadiri, C.D. Barrett, J. Wang, C.N. Tomé, Why are {101¯2} twins profuse in magnesium? Acta Mater. 85 (2015) 354–361.
[54] M. Niewczas, K. Noble, A. Kula, R.K. Mishra, Plasticity of Mg–Gd alloys between 4 K and 298 K, Philos. Mag. 96 (2) (2016) 134–165.
[55] L. Capolungo, I.J. Beyerlein, Nucleation and stability of twins in hcp metals, Phys. Rev. B 78 (2) (2008).
[56] J. Wang, I.J. Beyerlein, C.N. Tomé, An atomic and probabilistic perspective on twin nucleation in Mg, Scr. Mater. 63 (7) (2010) 741–746.
[57] J. Wang, J.M. Molina-Aldareguía, J. Llorca, Effect of Al content on the critical resolved shear stress for twin nucleation and growth in Mg alloys, Acta Mater. 188 (2020) 215–227.
[58] M.R. Barnett, M.D. Nave, A. Ghaderi, Yield point elongation due to twinning in a magnesium alloy, Acta Mater. 60 (4) (2012) 1433–1443.
[59] C.D. Barrett, H. El Kadiri, The roles of grain boundary dislocations and disclinations in the nucleation of {102} twinning, Acta Mater. 63 (2014) 1–15.
[60] M. Arul Kumar, I.J. Beyerlein, C.N. Tomé, Effect of local stress fields on twin characteristics in HCP metals, Acta Mater. 116 (2016) 143–154.
[61] J. Jiang, T.B. Britton, A.J. Wilkinson, Evolution of dislocation density distributions in copper during tensile deformation, Acta Mater. 61 (19) (2013) 7227–7239.
[62] A. Duckham, R.D. Knutsen, O. Engler, Influence of deformation variables on the formation of copper-type shear bands in Al–1Mg, Acta Mater. 49 (14) (2001) 2739–2749.
[63] K.D. Molodov, T. Al-Samman, D.A. Molodov, Profuse slip transmission across twin boundaries in magnesium, Acta Mater. 124 (2017) 397–409.